Properties of the remnant disk and the dynamical ejecta produced in low-mass black hole-neutron star mergers

Kota Hayashi[1], Kyohei Kawaguchi,[2] Kenta Kiuchi[3,1] Koutarou Kyutoku,[4,1,5] and Masaru Shibata[3,1]

[1]*Center for Gravitational Physics, Yukawa Institute for Theoretical Physics, Kyoto University, Kyoto 606-8502, Japan*
[2]*Institute for Cosmic Ray Research, The University of Tokyo, 5-1-5 Kashiwanoha, Kashiwa, Chiba 277-8582, Japan*
[3]*Max Planck Institute for Gravitational Physics (Albert Einstein Institute), Am Mühlenberg 1, Postdam-Golm 14476, Germany*
[4]*Department of Physics, Kyoto University, Kyoto 606-8502, Japan*
[5]*Interdisciplinary Theoretical and Mathematical Sciences Program (iTHEMS), RIKEN, Wako, Saitama 351-0198, Japan*

We systematically perform numerical-relativity simulations for low-mass black hole-neutron star mergers for the models with seven mass ratios $Q = M_{BH}/M_{NS}$ ranging from 1.5 to 4.4, and three neutron-star equations of state, focusing on the properties of matter remaining outside the black hole and ejected dynamically during the merger. We pay particular attention to the dependence on the mass ratio of the binaries. It is found that the rest mass remaining outside the apparent horizon after the merger depends only weakly on the mass ratio for the models with low mass ratios. It is also clarified that the rest mass of the ejecta has a peak at $Q \sim 3$, and decreases steeply as the mass ratio decreases for the low mass-ratio case. We present a novel analysis method for the behavior of matter during the merger, focusing on the matter distribution in the phase space of specific energy and specific angular momentum. Then we model the matter distribution during and after the merger. Using the result of the analysis, we discuss the properties of the ejecta.

I. INTRODUCTION

The era of the gravitational-wave astronomy was opened by the first detection of a binary black hole merger GW150914 [1]. For the event GW170817 [2], the electromagnetic counterpart signals were successfully detected [3,4]. It is widely believed that the source of GW170817 is the merger of binary neutron stars. However, the fact that became clear about the source of GW170817 is limited as follows. The observation of gravitational waves indicates that the component masses are 1.36–1.89 $M_\odot$ and 1.00–1.36 $M_\odot$ [5]. The observations of a short gamma-ray burst GRB 170817A and a kilonova/macronova AT 2017gfo by electromagnetic waves indicate that matter is involved in the merger process and at least one of the compact objects composing the binary is a neutron star. On the basis of these observational facts, however, the possibility of the source being a black hole-neutron star merger is not completely excluded [6,7]. In addition, GW190425, an event detected in 2019, is analyzed to be gravitational waves radiated from the merger of binary compact objects, the component masses of which are 1.61–2.52 $M_\odot$ and 1.12–1.68 $M_\odot$ [8]. It has not been determined whether the source is a black hole-neutron star merger or a binary

neutron star merger for this event either [9,10]. Including these two events, there are increasing numbers of gravitational-wave events and some of them are thought to include neutron stars [11,12], but the source objects of these events are not strongly constrained.

In order to determine the properties of the sources, it is crucial to understand the behavior of the system theoretically. High-accuracy gravitational-wave templates are needed for the parameter estimation after the detection of gravitational waves, and models for electromagnetic emissions are essential tools for analyzing electromagnetic counterpart signals. The key quantities for determining electromagnetic emissions include the remnant disk mass, the ejecta mass, and the ejecta velocity. Here, the ejecta is the matter which becomes unbound from the system. R-process nucleosynthesis in the neutron-rich matter such as the matter outflowed from the remnant accretion disk and the dynamically ejected matter is expected to power an electromagnetic transient kilonova/macronova [13,14]. Also, the compact object surrounded by an accretion disk has been proposed as a likely candidate for the central engine of short gamma-ray bursts (see Refs. [15,16] for reviews).

A variety of numerical-relativity simulations have been performed for black hole-neutron star binaries [6,7,17–45],

043007-1

and quantitative dependence of the merger behavior on binary parameters has been extensively studied. Some work took into account magnetic fields [28,32,33,38,40,44], nuclear-theory-based equations of state (EOSs) [6,7,19, 20,29,36,37,39–43,45], neutrino cooling [6,7,36,37, 41–43], neutrino heating [42], and misalignment of the black-hole spin with respect to the orbital angular momentum [30,34,39,41]. However, previous studies on the black hole-neutron star mergers which took nuclear-theory-based EOSs into account focused primarily on the system with a black-hole mass larger than 5 $M_\odot$. There are only a small number of studies carried out for low-mass black hole-neutron star mergers with black-hole mass of 2–3 $M_\odot$ [45]. This is because the black-hole mass observed in our galaxy was in the range of 5–20 $M_\odot$ [46], and a black hole with a mass lower than ~3 $M_\odot$ was not highly expected to exist. However, recent electromagnetic observations are indicating the existence of a compact object with mass ~3.3 $M_\odot$ [47]. Also, some gravitational-wave event candidates indicate the existence of a compact object with mass in the range of the mass gap of 2–5 $M_\odot$ [48,49]. In this situation, extensive theoretical studies on low-mass black hole-neutron star mergers are urgently needed.

In the present study, we perform numerical relativity simulations of non-spinning low-mass black hole-neutron star mergers. The simulations were performed systematically in order to study the parameter dependence of the merger remnant of the system. Specifically, the simulations are performed for seven initial black-hole mass $M_{BH} = 2.0$, 2.5, 3.0, 3.5, 4.0, 5.0, and 6.0 $M_\odot$ and three neutron-star EOSs while fixing the neutron-star mass to be 1.35 $M_\odot$. We pay particular attention to the rest mass remaining outside the apparent horizon after the merger, the ejecta mass, and the ejecta velocity.

This paper is organized as follows. In Sec. II, we briefly summarize the method for the numerical simulation and the diagnostics. In Sec. III, we present the numerical results obtained from the simulations focusing on the dependence of the rest mass remaining outside the apparent horizon after the merger, the ejecta mass, and the ejecta velocity on the mass ratio and the neutron-star EOS. Finally, a conclusion of this work is presented in Sec. IV. Throughout this paper, we adopt the geometrical units in which $G = c = 1$, where G and c are the gravitational constant and the speed of light, respectively. Our convention of notation is summarized in Table I. The compactness of the neutron star, the total mass of the system at infinite separation, and the mass ratio of the binary are defined as $\mathcal{C} := M_{NS}/R_{NS}$, $m_0 := M_{BH} + M_{NS}$, and $Q := M_{BH}/M_{NS}$, respectively. Latin and Greek indices denote spatial and spacetime components, respectively.

II. METHODS

In this section, we present methods for the numerical simulation. The details of the formulation, the gauge

TABLE I. Our convention of notation for physically important quantities, geometric variables, and hydrodynamic variables.

Symbol	
M_{BH}	Gravitational mass of the black hole in isolation
a_{BH}	Kerr parameter of the black hole
χ_{BH}	Dimensionless spin parameter of the black hole
M_{NS}	Gravitational mass of the neutron star in isolation
R_{NS}	Circumferential radius of the neutron star in isolation
$\mathcal{C}$	Compactness parameter of the neutron star: M_{NS}/R_{NS}
m_0	Total mass of the system at infinite separation
Q	Mass ratio of the binary: M_{BH}/M_{NS}
γ_{ij}	Induced metric on a $t = $ const hypersurface
α	Lapse function
β^i	Shift vector
γ	Determinant of γ_{ij}
ρ	Baryon rest-mass density
u^μ	Four velocity of the fluid
P	Pressure
ε	Specific internal energy
h	Specific enthalpy: $1 + \varepsilon + P/\rho$
ρ_*	Conserved baryon rest-mass density: $\rho\alpha\sqrt{\gamma}u^t$
$\hat{e}$	Specific energy: $h\alpha u^t - P/\rho\alpha u^t$

conditions, the numerical scheme, and the initial data computation are described in Refs. [17,18,20,39].

A. Dynamical simulation

Numerical simulations are carried out by using the SACRA-MPI code [50]. This code employs an adaptive-mesh-refinement (AMR) method to save the computational cost [51] and MPI/OpenMP hybrid parallelization to speed up the computation [50]. SACRA solves the Einstein equation in a moving puncture version [52–54] of the Baumgarte-Shapiro-Shibata-Nakamura (BSSN) formulation [55,56], incorporating a Z4c constraint-propagation prescription locally [57]. Together with the Einstein equation, we solve pure hydrodynamics equations in this paper. Magnetohydrodynamics or neutrino effects are not taken into account because we focus on the dynamics of the system up to ~15 ms after the merger.

In this work, we prepare ten refinement levels for the AMR computational domain. Specifically, two sets of four finer domains comoving with either the black hole or the neutron star cover the region of their vicinity. The other six coarser domains cover both the black hole and the neutron star by a wider domain with their origins fixed at the center of the mass of the binary system.

B. Zero-temperature EOS

The temperature of the neutron star, except for the newly born ones and the massive neutron star produced after the merger of binary neutron stars, can be approximated as zero because the cooling time scale of a neutron star is much

TABLE II.   The EOS parameter adopted in this study. M_{max} is the maximum gravitational mass of the spherical neutron star for each EOS. $R_{1.35}$ and $\mathcal{C}_{1.35}$ are the radius and the compactness for a neutron star with the gravitational mass 1.35 $M_{\odot}$, respectively.

EOS	$\log_{10}P_{\mathrm{fid}}$ [dyne/cm²]	M_{max} [$M_{\odot}$]	$R_{1.35}$ [km]	$\mathcal{C}_{1.35}$
1.25H	34.6	2.383	13.0	0.154
H	34.5	2.249	12.3	0.162
HB	34.4	2.122	11.6	0.172

shorter than the lifetime of typical compact binaries [58]. With a zero-temperature EOS, thermodynamical quantities such as pressure P, specific internal energy ε, and specific enthalpy h are written as a function of rest-mass density ρ. In this study we employ a piecewise polytropic EOS with two pieces as [59–61]

$$P_{\mathrm{cold}}(\rho) = K_i \rho^{\Gamma_i} (\rho_{i-1} < \rho < \rho_i, \quad i = 1, 2) \quad (1)$$

where $\rho_0 = 0$, ρ_1 is of order 10^{14} g cm^{-3} (see below), and $\rho_2 = \infty$. Below ρ_1, we adopt $K_1 = 3.5966 \times 10^{13}$ in cgs unit, $\Gamma_1 = 1.3569$, and for $\rho \geq \rho_1$, we adopt $\Gamma_2 = 3.0$. The remaining free parameters are K_2 and ρ_1. These are determined by choosing pressure P_{fid} at certain fiducial density $\rho_{\mathrm{fid}} = 10^{14.7}$ g cm^{-3} as $K_2 = P_{\mathrm{fid}}/\rho_{\mathrm{fid}}^{\Gamma_2}$ and by requiring the continuity of the pressure as $\rho_1 = (K_2/K_1)^{1/(\Gamma_1 - \Gamma_2)}$. We choose three EOSs shown in Table II in order to

investigate the EOS dependence of the merger outcome of the binary systems. These selected EOSs satisfy the constraints $\Lambda_{1.4} \lesssim 800$ imposed by the observation of GW170817 [2]. Here, $\Lambda_{1.4}$ is the dimensionless tidal deformability for an isolated neutron star with the gravitational mass 1.4 $M_{\odot}$. Also with these EOSs, the maximum mass for the spherical neutron stars, M_{max} is higher than 2.1 $M_{\odot}$, which is consistent with the latest discoveries of a high-mass neutron star [62]. In the numerical simulation, we add the thermal part of the EOS to the zero-temperature part described above. Our implementation for this is the same as that in our previous work (see, e.g., Ref. [39]).

C. Model

The neutron-star mass is set to be 1.35 $M_{\odot}$ with the vanishing black-hole spin for all the models. In order to investigate the mass-ratio dependence of the system evolution, we choose seven mass ratios $Q \approx 1.5$, 1.9, 2.2, 2.6, 3.0, 3.7, and 4.4, that is, we choose the black-hole mass $M_{\mathrm{BH},0} = 2.0$, 2.5, 3.0, 3.5, 4.0, 5.0, and 6.0 $M_{\odot}$. As mentioned above, we also choose three EOSs 1.25H, H, and HB. The 19 physical models employed in this study are listed in Table III. Strictly speaking, the neutron star EOS with $M_{\mathrm{max}} > 2.1$ $M_{\odot}$ and $M_{\mathrm{BH}} = 2$ $M_{\odot}$ are astrophysically unlikely. However, we adopt this value because the main focus of this paper is to understand the low-mass black hole-neutron star merger process.

TABLE III.   Key parameters and quantities for the initial conditions adopted in our numerical simulations. The adopted EOS, the compactness of the neutron star $\mathcal{C}$, and the initial black-hole mass $M_{\mathrm{BH},0}$ are shown. Note that $M_{\mathrm{NS}} = 1.35$ $M_{\odot}$ and the initial black-hole spin is zero. $m_0\Omega_0$, $M_{\mathrm{ADM},0}$, and $J_{\mathrm{ADM},0}$ are the initial dimensionless orbital angular velocity, Arnowitt-Deser-Misner (ADM) mass, and ADM angular momentum of the system, respectively. Δx is the grid spacing for the highest resolution model N110 and L is the size of the computational domain.

Model	EOS	$\mathcal{C}$	$M_{\mathrm{BH},0}$ [$M_{\odot}$]	$m_0\Omega_0$	$M_{\mathrm{ADM},0}$ [$M_{\odot}$]	$J_{\mathrm{ADM},0}$ [$M_{\odot}^2$]	Δx [m]	L [km]
125H_Q15	1.25H	0.154	2.0	0.024	3.33	10.63	127	7206
125H_Q19	1.25H	0.154	2.5	0.024	3.83	13.27	124	7006
125H_Q22	1.25H	0.154	3.0	0.024	4.33	15.90	124	7006
125H_Q26	1.25H	0.154	3.5	0.024	4.83	18.53	124	7006
125H_Q30	1.25H	0.154	4.0	0.024	5.34	21.15	124	7006
125H_Q37	1.25H	0.154	5.0	0.026	6.34	25.88	122	6906
125H_Q44	1.25H	0.154	6.0	0.026	7.35	30.97	122	6906
H_Q15	H	0.162	2.0	0.024	3.33	10.63	117	6606
H_Q19	H	0.162	2.5	0.024	3.83	13.27	117	6606
H_Q22	H	0.162	3.0	0.024	4.33	15.91	117	6606
H_Q26	H	0.162	3.5	0.024	4.83	18.53	117	6606
H_Q30	H	0.162	4.0	0.024	5.34	21.15	117	6606
H_Q37	H	0.162	5.0	0.026	6.34	25.88	113	6406
H_Q44	H	0.162	6.0	0.026	7.35	30.97	122	6406
HB_Q15	HB	0.172	2.0	0.024	3.33	10.63	109	6139
HB_Q19	HB	0.172	2.5	0.024	3.83	13.27	109	6139
HB_Q22	HB	0.172	3.0	0.024	4.33	15.91	109	6139
HB_Q26	HB	0.172	3.5	0.024	4.83	18.53	109	6139
HB_Q30	HB	0.172	4.0	0.024	5.34	21.15	109	6139

Initial data for our numerical simulations are obtained by computing a quasiequilibrium state of an orbiting black hole-neutron star binaries following Ref. [63]. Here, we assume that the neutron star is irrotational [64,65] and is modeled by zero-temperature EOSs (see Ref. [58] for reviews).

In order to confirm the reliability of the numerical results, we perform three simulations for every model listed above with different grid resolutions N70, N90, and N110. They resolve the neutron-star radius by about 50, 65, and 80 grid points on the finest AMR domain, respectively. The grid spacing for the highest-resolution model N110 is $\Delta x \approx 110$–130 m for EOS 125H, H, and HB on the finest AMR domain. Unless otherwise stated, the numerical results obtained from the simulations of N110 are presented for each model.

D. Diagnostics

1. Remnant disk and ejecta

The fate of the neutron-star matter after merger is divided into three types. The matter that falls immediately into the black hole, the matter that forms an accretion disk, and the matter that becomes unbound from the system, i.e., ejecta. Here, we describe our method to evaluate the properties of the disk and the ejecta, which are the key quantities for the electromagnetic emissions from black hole-neutron star mergers. At each time slice, the rest mass outside the apparent horizon is evaluated by the integral

$$M_{>\mathrm{AH}} := \int_{r > r_{\mathrm{AH}}} \rho_* d^3 x, \qquad (2)$$

where $r_{\mathrm{AH}} = r_{\mathrm{AH}}(\theta, \varphi)$ is the coordinate radius of the apparent horizon with θ and φ being the polar angles defined in a black-hole centered frame. Here, we define the time at the onset of merger t_{merger} as the time at which $10^{-2} M_\odot$ of neutron-star matter falls into the apparent horizon. In Sec. III, we present the values of $M_{>\mathrm{AH}}$ evaluated at 12 ms after the onset of merger.

The ejecta, which is the matter unbound from the system, is defined as the matter that satisfies $-u_t > 1$.[1] The mass of the ejecta is defined by integrating the conserved rest-mass density of the matter with $-u_t > 1$ as

$$M_{\mathrm{eje}} := \int_{-u_t > 1, r > r_{\mathrm{AH}}} \rho_* d^3 x. \qquad (3)$$

---

[1]If we consider the thermal effect, the criterion for the unbound matter should be expressed as $-hu_t > 1$. For the dynamical ejecta produced in the merger of black hole-neutron star binaries, matter is ejected mainly due to the tidal force and it does not experience the shock heating. Therefore, numerical results in this paper depend only weakly on the choice of the criterion.

The average velocity of the ejecta is defined by considering the kinetic energy of the ejecta. First, a sum of the rest-mass, internal, and kinetic energies of the ejecta is defined by

$$E_{\mathrm{eje}} := \int_{-u_t > 1, r > r_{\mathrm{AH}}} \rho_* \hat{e} d^3 x, \qquad (4)$$

where $\hat{e}$ is defined in Table I. Next, the internal energy of the ejecta is defined by

$$U_{\mathrm{eje}} := \int_{-u_t > 1, r > r_{\mathrm{AH}}} \rho_* \varepsilon d^3 x. \qquad (5)$$

Then, the kinetic energy of the ejecta is defined by subtracting the rest-mass energy and internal energy from E_{eje} as

$$T_{\mathrm{eje}} := E_{\mathrm{eje}} - U_{\mathrm{eje}} - M_{\mathrm{eje}}. \qquad (6)$$

Subsequently, by assuming the Newtonian dynamics, average velocity of the ejecta may be evaluated from its kinetic energy and the mass as

$$v_{\mathrm{eje}} := \sqrt{\frac{2 T_{\mathrm{eje}}}{M_{\mathrm{eje}}}}. \qquad (7)$$

However, the values of E_{eje} and U_{eje} are evaluated for a computational domain of radius <6000–7000 km. Then, in E_{eje} (and thus T_{eje}), the influence on the gravitational potential energy remains. We must subtract the effect of this gravitational potential energy. Assuming the Newtonian gravity, we thus approximately estimate the extrapolated velocity as

$$v_{\mathrm{eje,extrap}} := \sqrt{v_{\mathrm{eje}}^2 - 2 \frac{m_0}{v_{\mathrm{eje}}(t - t_{\mathrm{merger}})}}, \qquad (8)$$

where v_{eje} is evaluated at t. In Sec. III, we also present the values of M_{eje} and v_{eje} evaluated at 12 ms after the onset of merger.

2. Black hole

Parameters of black holes are estimated by integrals on apparent horizons. By assuming that the spacetime is approximately stationary and the effect of matter would be negligible near the black hole, the equatorial circumferential radius C_{e} and the area A_{AH} of the apparent horizon approximately satisfy [26]

$$C_{\mathrm{e}} = 4\pi M_{\mathrm{BH}}, \qquad (9)$$

$$A_{\mathrm{AH}} = 8\pi M_{\mathrm{BH}} \left(M_{\mathrm{BH}} + \sqrt{M_{\mathrm{BH}}^2 - a_{\mathrm{BH}}^2} \right). \qquad (10)$$

Therefore, the black-hole mass M_{BH} and the dimensionless spin parameter χ_{BH} are approximately evaluated as

$$M_{BH} = \frac{C_e}{4\pi}, \tag{11}$$

$$\chi_{BH} = \frac{1}{M_{BH}} \sqrt{M_{BH}^2 - \left(\frac{A_{AH}}{8\pi M_{BH}} - M_{BH}\right)^2}. \tag{12}$$

Comparisons among different estimates of the spin parameter suggest that the systematic error associated with this method is smaller than 0.01 [17,18,26], and we confirmed that this also holds for simulations presented in this work. As in the case of the remnant disk and ejecta, in Sec. III, we present the mass and dimensionless spin of the black hole estimated at 12 ms after the onset of merger.

3. Orbital angular velocity

Here, we summarize the method for computing the orbital angular velocity from gravitational waves. We extract a Weyl scalar Ψ_4 at the coordinate radius of $D = 400\ M_\odot$ from the coordinate origin by projecting onto spin-weighted spherical harmonics, and extrapolate them to null infinity by a method based on the black-hole perturbation theory [66]. The gravitational waveforms h_{gw} are obtained from time integration of $l = 2, m = \pm 2$ modes of Ψ_4 [67]. The angular velocity of gravitational waves is derived by

$$\Omega_{gw} = -\frac{1}{|h_{gw}|^2} \text{Im}[h_{gw}^* \dot{h}_{gw}], \tag{13}$$

where h_{gw}^* and $\dot{h}_{gw}$ denotes the complex conjugate and the time derivative of h_{gw}, respectively. The orbital angular velocity of the binary Ω is estimated as $\Omega = \Omega_{gw}/2$ in a gauge-invariant manner. The retarded time is approximately defined by

$$t_{ret} := t - D - 2m_0 \ln(D/m_0). \tag{14}$$

Then we define the orbital angular velocity at the onset of merger as $\Omega_{merger} := \Omega(t_{ret} = t_{merger})$.

III. RESULTS

In this section, we present the results obtained from our numerical simulations. Key characteristic quantities are shown in Table IV (see also Appendix A for lower-resolution results).

A. Overview of the merger process

Here, we overview merger processes (see Ref. [68] for reviews). Gravitational radiation dissipates energy and angular momentum from black hole-neutron star binaries, and the orbital separation decreases leading to merger.

TABLE IV. Characteristic quantities of the remnant disk and the ejecta measured at 12 ms after the onset of merger for models with the highest resolution N110. $M_{>AH}$ is the rest mass outside the apparent horizon. M_{eje} is the rest mass of the ejecta. $v_{eje,extrap}$ is the average velocity of the ejecta extrapolated to $r \to \infty$. For low ejecta mass $<10^{-5}\ M_\odot$, we do not estimate the ejecta velocity.

Model	$M_{>AH}\ [M_\odot]$	$M_{eje}\ [M_\odot]$	$v_{eje,extrap}\ [c]$
125H_Q15	1.0×10^{-1}	3.7×10^{-4}	0.10
125H_Q19	1.0×10^{-1}	1.5×10^{-3}	0.12
125H_Q22	1.0×10^{-1}	2.9×10^{-3}	0.14
125H_Q26	9.1×10^{-2}	2.9×10^{-3}	0.14
125H_Q30	6.7×10^{-2}	3.8×10^{-3}	0.16
125H_Q37	1.4×10^{-2}	3.5×10^{-3}	0.18
125H_Q44	3.5×10^{-4}	6×10^{-5}	0.14
H_Q15	7.0×10^{-2}	3×10^{-5}	0.11
H_Q19	7.3×10^{-2}	3.9×10^{-4}	0.12
H_Q22	6.6×10^{-2}	8.8×10^{-4}	0.14
H_Q26	4.4×10^{-2}	9.0×10^{-4}	0.13
H_Q30	2.3×10^{-2}	2.0×10^{-3}	0.15
H_Q37	1.3×10^{-3}	2.3×10^{-4}	0.15
H_Q44	$<10^{-5}$	$<10^{-5}$	…
HB_Q15	3.7×10^{-2}	$<10^{-5}$	…
HB_Q19	3.9×10^{-2}	6×10^{-5}	0.16
HB_Q22	2.5×10^{-2}	9×10^{-5}	0.11
HB_Q26	1.6×10^{-2}	8.4×10^{-4}	0.14
HB_Q30	5.0×10^{-3}	5.2×10^{-4}	0.14

The fate of the system is divided broadly into two cases. One is that the neutron star is disrupted by the tidal force of the black hole. If this is the case, the remnant black hole is surrounded by an accretion disk, and a portion of the disrupted matter is ejected dynamically. This is the case which we are interested in, and most of our models result in this type. The other is that the neutron star is not tidally disrupted, and is simply swallowed by the black hole. This is the case for models with mass ratios $Q \gtrsim 4$–5. We do not pay particular attention to this case. The condition which discriminates these two cases is approximately obtained by comparing the orbital separation at which tidal disruption occurs and the radius of the innermost stable circular orbit of the system.

Figure 1 plots the snapshots of the rest-mass density profiles, unbound components, and the location of the apparent horizon on the equatorial plane for the model H_Q22. At $t - t_{merger} \approx -1.5$ ms, the binary is in the inspiral stage, and the neutron star is not deformed appreciably. At $t - t_{merger} \approx 0.0$ ms, the binary is in the merger stage, and the neutron star is highly deformed by the tidal force of the black hole. Subsequently, the merger occurs and $\sim 95\%$ of the neutron-star matter falls into the black hole, while $\sim 5\%$ of the matter remains outside the black hole. At $t - t_{merger} \approx 1.5$ ms, we observe a one-armed spiral structure

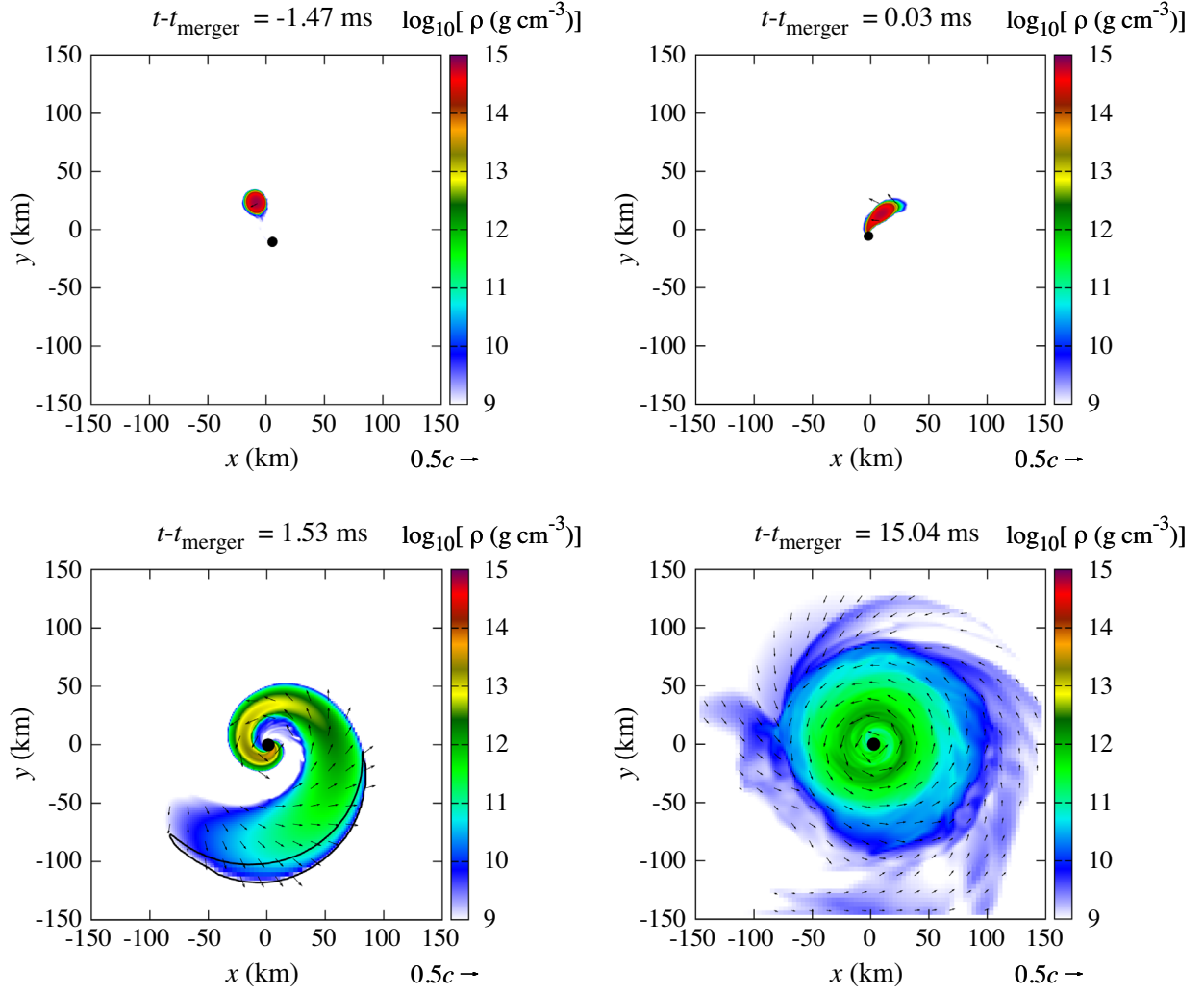FIG. 1. Time evolution of the rest-mass density profile at $t - t_{\mathrm{merger}} \approx -1.5$ (top left), 0.0 (top right), 1.5 (bottom left), and 15.0 ms (bottom right) for the model H_Q22. The black filled circles indicate the interior of the apparent horizons. Unbound components that satisfy $-u_t \geq 1$ are enclosed by the black curves (see the bottom left panel). The black arrows show the three-velocity, $v^i := u^i/u^t$.

for the matter located outside the innermost stable circular orbit of the black hole as a result of tidal disruption. A large portion of the arm is kept bound to the remnant black hole, and hence, they will experience fallback and result in the formation of an accretion disk around the remnant black hole. On the other hand, a small portion of the arm at the front side acquires specific energy that satisfies $-u_t \geq 1$ and becomes ejecta. At $t - t_{\mathrm{merger}} \approx 15.0$ ms, the accretion disk with the maximum density of $\sim 10^{12}$ g cm^{-3} is formed around the remnant black hole. A large portion of the disrupted matter is in a circular motion and the system relaxes to a quasisteady state.

B. Rest mass remaining outside the apparent horizon after the merger

Figure 2 shows the dependence of the rest mass remaining outside the apparent horizon after the merger,

$M_{>\mathrm{AH}}$, on the binary parameters. First, we pay attention to the dependence of $M_{>\mathrm{AH}}$ on the EOS. As we find from Fig. 2 and Table IV, $M_{>\mathrm{AH}}$ increases as the compactness of the neutron star decreases. This dependence was already shown by previous simulations [17] and reflects the fact that the neutron star with a larger radius is tidally disrupted at a more distant orbit.

Next, we pay attention to the dependence of $M_{>\mathrm{AH}}$ on the mass ratio of binary. Figure 2 shows that for high mass ratios ($Q \gtrsim 3$), $M_{>\mathrm{AH}}$ increases as the mass ratio decreases. This dependence was also already shown in previous simulations for a higher mass-ratio regime [26]. However, for a low mass ratio ($Q \lesssim 3$), the dependence of $M_{>\mathrm{AH}}$ on the mass ratio becomes very weak. This behavior was not expected from the mass-ratio dependence for the higher mass-ratio regime. It was already pointed out by Foucart *et al.* [6] that for a low-mass-ratio regime $M_{>\mathrm{AH}}$
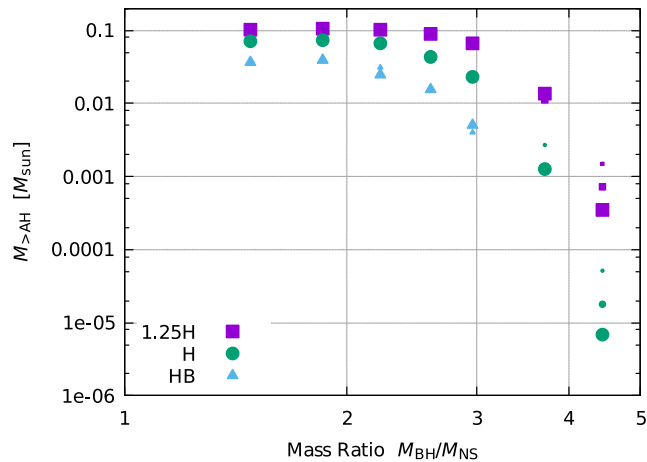
FIG. 2. Rest mass remaining outside the apparent horizon after the merger, $M_{>AH}$, as a function of the mass ratio Q for three EOSs. Data are evaluated at 12 ms after the onset of merger. Data points with different sizes show results obtained with different grid resolutions. Specifically, large, medium, and small points show the results of N110, N90, and N70, respectively.

tends to be smaller than previously predicted in Ref. [69]. Our work systematically shows that $M_{>AH}$ becomes approximately constant irrespective of the mass ratio.

In Appendix B, we also reanalyze the results of our previous numerical simulations for models with higher mass ratios and spinning black holes [18,20]. It is shown that the tendency similar to that shown in Fig. 2 is found for these previous results.

C. Ejecta properties

One of the important quantities that characterize ejecta is its mass. Figure 3 shows the dependence of the ejecta mass M_{eje} on the mass ratio and neutron-star EOS. It
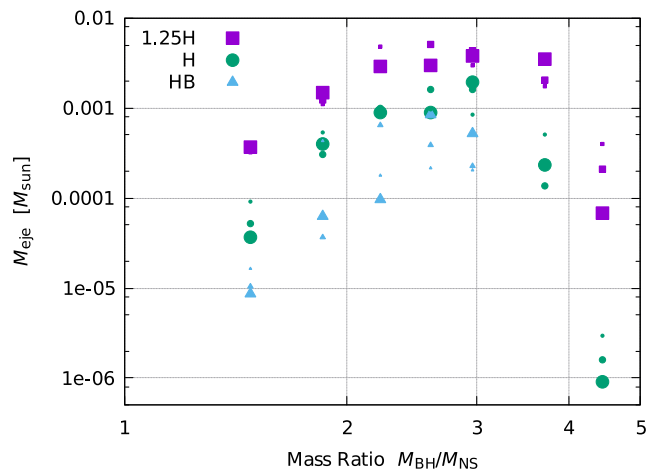
is found that as in the case of the rest mass remaining outside the apparent horizon after the merger, M_{eje} increases as the compactness of the neutron star decreases. This dependence is consistent with the results in the previous work for higher mass ratios [20].

For the models with the mass ratio higher than ~ 3, M_{eje} decreases as the mass ratio increases. This dependence is in agreement with the rapid drop of the rest mass remaining outside the apparent horizon after the merger at the higher mass-ratio regime. This is also consistent with the results in the previous work [20]. However, for the models with the mass ratio lower than ~ 3, the situation changes. M_{eje} decreases as the mass ratio decreases for the parameters employed in our simulation. This behavior is consistent with the numerical results in Ref. [6], which show that there is little unbound matter produced by a merger in the near-equal-mass regime. Overall, we systematically show that M_{eje} exhibits a peak at the mass ratio ~ 3. However, it is not evident that the peak always exists for the cases that are not explored in this work. The peak mass ratio could depend on the neutron-star EOS and the black-hole spin. Further study is needed to reveal whether the peak always exists or not.

Ejecta velocity is another important quantity that characterizes the ejecta. Figure 4 shows the extrapolated ejecta velocity $v_{eje,extrap}$ as a function of Q for three EOSs. We also show $v_{eje,extrap}$ for the models simulated in previous studies (see the small open circles, for which the data are taken from Table 2 of Ref. [70]). This figure shows that $v_{eje,extrap}$ tends to decrease as the mass ratio of binary decreases. By contrast, the dependence on neutron-star EOSs is likely to be weak. This result is consistent with the results obtained in the merger of binaries consisting of spinning black holes [20,70].
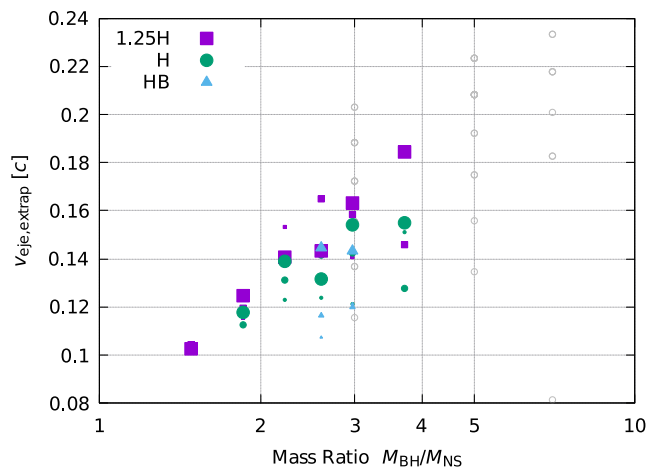

FIG. 3. The same as Fig. 2 but for the rest mass of unbound material, M_{eje}, as a function of the mass ratio Q.

FIG. 4. The same as Fig. 2 but for the average velocity of the ejecta extrapolated to $r \to \infty$, $v_{eje,extrap}$, as a function of the mass ratio Q. The results for the models with the ejecta mass larger than 10^{-4} $M_\odot$ are plotted. Data are evaluated at 12 ms after the onset of merger. Results from Ref. [70] are also shown (small open circles). Note that data in Ref. [70] are evaluated at 10 ms after the onset of merger.

D. Considerations on the mass ejection

In Sec. III C we showed the main results of our simulations for the rest mass and the velocity of the ejecta. The mass-ratio dependence of the ejecta properties is summarized as follows.

  (i) The ejecta mass increases as the mass ratio decreases for a high mass-ratio regime, while it decreases as the mass ratio decreases for a low mass-ratio regime. The peak of the ejecta mass is found at $Q \sim 3$.
 (ii) The ejecta velocity decreases as the mass ratio decreases.

In this section, we consider the mechanism of mass ejection and give our interpretation for the mass-ratio dependence of the properties of the ejecta.

1. Matter distribution in the energy-angular momentum phase space

In order to take a close look at the dynamics of the merger and explain the mass-ratio dependence of the ejecta mass, we analyze the matter distribution in the phase space of specific energy and specific angular momentum. Figure 5 shows the time evolution of the distribution in the phase space of specific energy $\tilde{E} := -u_t$ and specific angular momentum $\tilde{J} := u_\varphi = u_y(x - x_{\text{BH}}) - u_x(y - y_{\text{BH}})$ for the models with EOS H. Here, $\tilde{E}$ and $\tilde{J}$ can be understood as the Killing energy and the Killing angular momentum, respectively, if we assume the stationary, axisymmetric spacetime. The matter distribution is obtained by the following integral:

$$\frac{dM}{d\tilde{E}d\hat{J}}(\tilde{E}, \hat{J}) := \lim_{\Delta_1, \Delta_2 \to 0} \frac{1}{\Delta_1 \Delta_2} \int_{\substack{|\tilde{E}-\tilde{E}'|<0.5\Delta_1 \\ |\hat{J}-\hat{J}'|<0.5\Delta_2}} \rho_*(\tilde{E}', \hat{J}')d^3x, \quad (15)$$

where $\hat{J} := \tilde{J}/M_{\text{BH,f}}$, and $M_{\text{BH,f}}$ is the mass of the remnant black hole. From each panel of Fig. 5, we can extract the following information for the inspiral, merger, and post-merger stages:

  (1) *Inspiral stage* The first panel of Fig. 5 shows the matter distribution in the phase space for the late inspiral stage just prior to the merger. The upper limit of the specific energy for each specific angular momentum can be described approximately by $\tilde{E} = \Omega\tilde{J} + C$, where Ω is an orbital angular velocity and C is a constant (at each time slice) in the presence of a helical symmetry.[2] The figure shows that most components have values of $\hat{J}$ smaller than $\hat{J}_{\text{ISCO}}$ and will fall into the black hole after the merger.
  (2) *The onset of merger* The second panel of Fig. 5 shows the matter distribution in the phase space at the onset of merger. This shows that the matter

acquires a wide range of specific angular momentum and a fraction of the matter has the specific angular momentum satisfying $\hat{J} \geq \hat{J}_{\text{ISCO}}$. This can be understood as a result of the angular momentum transport caused by the tidal deformation of the neutron star. The associated increase and decrease of the specific energy can also be observed. Note that the upper limit of the distribution approximately follows $\tilde{E} = \Omega\tilde{J} + C$ as with the case of the inspiral stage but with different values of Ω and C.

  (3) *1.5 ms after the onset of merger* The third panel of Fig. 5 shows the matter distribution in the phase space after the onset of tidal disruption of the neutron star. Compared with the second panel, the matter with $\hat{J} < \hat{J}_{\text{ISCO}}$ falls into the black hole and disappears from the drawing range. The specific energy of the matter that remains outside the black hole increases, while the specific angular momentum does not change significantly from the onset of merger. Therefore, the major effect in this stage is the change in the specific energy by the radial force acting on the matter. The matter acquires energy when the large portion of neutron-star matter falls into the black hole and the spacetime structure changes significantly (e.g., the quadrupole moment should be significantly reduced). The time duration for the matter to acquire energy is 0.5–1 ms. We speculate that the instantaneous change in the structure of the spacetime increases the specific energy of a portion of the matter.

  (4) *Quasisteady state after merger* The last panel of Fig. 5 shows the matter distribution in the phase space for a quasisteady state established after the merger. There are two components observed in this figure. One is the component that has noncircular orbits around the black hole (i.e., $\tilde{E}$ has large values for a given value of $\hat{J}$). The phase-space distribution of this component does not change significantly from ≈ 1.5 ms after the onset of merger. The other is the component that has a circular or nearly circular orbit around the black hole (the components along the magenta dashed curve). This constitutes the disk surrounding the black hole. Due to fallback and matter interaction in the disk, the angular momentum distribution of the latter component is changed significantly from ≈ 1.5 ms after the onset of merger.

2. Model for matter distribution in the specific energy-angular momentum phase space

In order to deeply understand the numerical results in this paper, we here develop a model for the phase-space distribution of the matter after merger using the effective potential of the remnant black hole, and compare it with the results of numerical simulations in Fig. 5. We first consider the phase-space distribution of the matter at ≈ 1.5 ms after the onset of merger. For the analysis, we assume the following:

---

[2]$h\tilde{E} = \Omega h\tilde{J} + C$ is satisfied if we assume the helical symmetry and irrotational fluid [63]. Here, the helical Killing vector is written as $\xi^\mu := (\partial_t)^\mu + \Omega(\partial_\varphi)^\mu$. Therefore, $\tilde{E} = \Omega\tilde{J} + C/h \leq \Omega\tilde{J} + C$ holds.
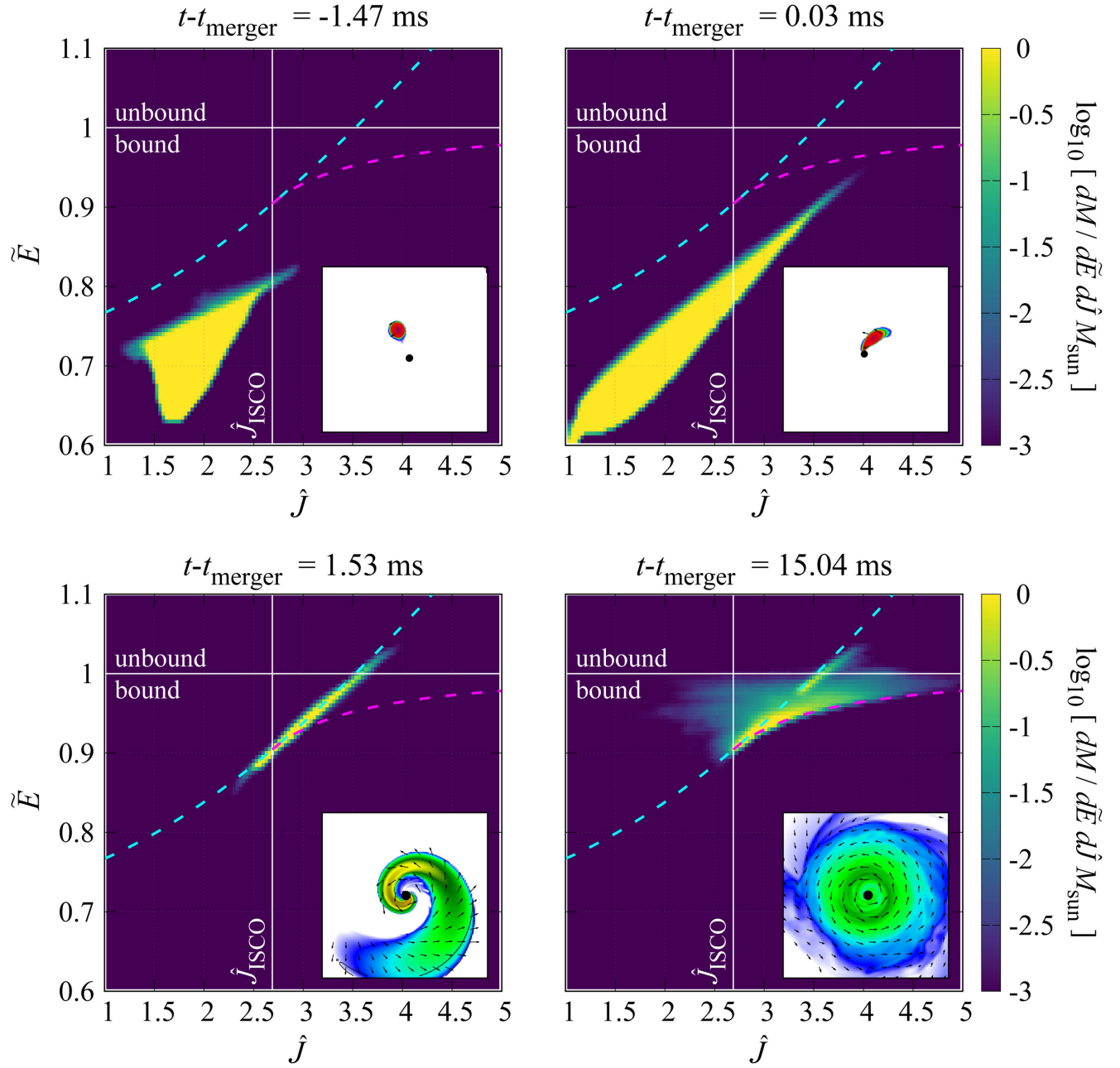
FIG. 5.   Time evolution of the matter distribution in the phase space of specific energy $\tilde{E} = -u_t$ and specific angular momentum normalized by the remnant black-hole mass $\hat{J} = u_\varphi/M_{\mathrm{BH,f}}$ at $t - t_{\mathrm{merger}} \approx -1.5$, 0.0, 1.5, and 15.0 ms for the model H_Q22. The contours are obtained by using Eq. (15). The cyan dashed curve describes $\tilde{E} = V_{\mathrm{eff}}(\hat{J})$ [Eq. (16)]. This curve shows the effective potential of Kerr spacetime at the orbital angular velocity Ω_{merger}. The values of the black-hole mass M_{BH} and the black-hole spin χ_{BH} used to evaluate Eq. (16) are given in Table V. The magenta dashed curve describes $(\tilde{E}, \hat{J}) = (\tilde{E}_{\mathrm{sco}}, \hat{J}_{\mathrm{sco}})$ [Eq. (18)]. This curve shows the relation of the specific energy and the specific angular momentum at stable circular orbits in the Kerr spacetime. $\hat{J}_{\mathrm{ISCO}}$ is the specific angular momentum at the innermost stable circular orbit around the remnant black hole normalized by its mass. The matter with $\hat{J} < \hat{J}_{\mathrm{ISCO}}$ falls into the black hole during the merger stage, while the matter with $\hat{J} > \hat{J}_{\mathrm{ISCO}}$ remains outside the black hole and forms a remnant disk or ejecta. The horizontal line of $\tilde{E} = 1$ is the boundary of the bound and unbound matter. The matter with $\tilde{E} > 1$ is unbound from the system and becomes ejecta. In each figure, the snapshot of the rest-mass density profile at the corresponding time slice is embedded. See Fig. 1 for the details of the snapshots.

(i) The matter motion after merger is determined only by the gravitational effects of the remnant black hole. The mass and the dimensionless spin of the remnant black holes are denoted by $M_{\rm BH,f}$ and $\chi_{\rm BH,f}$, respectively, and they are listed in Table V.

(ii) All the fluid elements follow the geodesic in the Kerr spacetime starting from the radial position $r_{\rm merger}/M_{\rm BH,f} = ((\Omega_{\rm merger}M_{\rm BH,f})^{-1} - \chi_{\rm BH,f})^{2/3}$ in Boyer-Lindquist coordinates, with the zero radial

velocity, $dr/d\tau = 0$, where $\Omega_{\rm merger}$ is the orbital angular velocity at the onset of merger and τ is the proper time of the fluid elements. $\Omega_{\rm merger}$ and $\hat{r}_{\rm merger} := r_{\rm merger}/M_{\rm BH,f}$ are also listed in Table V. This table shows that the value of $\Omega_{\rm merger}$ is primarily determined by the EOS and depends only weakly on the mass ratio.

Under these assumptions, the relation between the specific energy and the specific angular momentum is given by

$$\tilde{E} = V_{\rm eff}(\hat{J}) = V_+(\hat{r}_{\rm merger}, \hat{J}),$$

$$V_\pm(\hat{r}, \hat{J}) := \frac{2\chi_{\rm BH,f}\hat{J} \pm (\hat{r}^2 + \chi_{\rm BH,f}{}^2 - 2\hat{r})^{\frac{1}{2}}[\hat{J}^2\hat{r}^2 + \hat{r}(\hat{r}^3 + \chi_{\rm BH,f}{}^2\hat{r} + 2\chi_{\rm BH,f}{}^2)]^{\frac{1}{2}}}{\hat{r}^3 + \chi_{\rm BH,f}{}^2(\hat{r} + 2)}, \tag{16}$$

where $\hat{r} := r/M_{\rm BH,f}$. We note that $V_\pm(\hat{r}, \hat{J})$ is obtained from an effective potential of the geodesic (radial) motion around a Kerr black hole written in the form [71]

$$\left(\frac{dr}{d\tau}\right)^2 + V(\hat{r}, \tilde{E}, \tilde{J}) = 0,$$

$$V(\hat{r}, \tilde{E}, \tilde{J}) := \frac{1}{\hat{r}^3}[\{\hat{r}^3 + \chi_{\rm BH,f}{}^2(\hat{r} + 2)\}\tilde{E}^2 + (2 - \hat{r})\hat{J}^2 - 4\chi_{\rm BH,f}\tilde{E}\hat{J} - \hat{r}^2(\hat{r} - 2) - \chi_{\rm BH,f}{}^2\hat{r}]$$

$$= \left\{1 + \frac{\chi_{\rm BH,f}{}^2}{\hat{r}^3}(\hat{r} + 2)\right\}\{\tilde{E} - V_+(\hat{r}, \hat{J})\}\{\tilde{E} - V_-(\hat{r}, \hat{J})\}. \tag{17}$$

TABLE V. Quantities used in the model given by Eq. (16). $M_{\rm BH,f}$ and $\chi_{\rm BH,f}$ are the mass and the dimensionless spin of the remnant black hole, respectively. $\Omega_{\rm merger}$ is the orbital angular velocity at the onset of merger, and $\hat{r}_{\rm merger}$ is the radial position of matter in Boyer-Lindquist coordinates obtained from $\Omega_{\rm merger}$.

Model	$M_{\rm BH,f}$ $[M_\odot]$	$\chi_{\rm BH,f}$	$\Omega_{\rm merger}$ $[M_\odot^{-1}]$	$\hat{r}_{\rm merger}$
125H_Q15	3.20	0.75	2.24×10^{-2}	5.59
125H_Q19	3.68	0.69	2.27×10^{-2}	5.02
125H_Q22	4.17	0.64	2.27×10^{-2}	4.62
125H_Q26	4.67	0.59	2.30×10^{-2}	4.24
125H_Q30	5.18	0.56	2.29×10^{-2}	3.95
125H_Q37	6.21	0.50	2.24×10^{-2}	3.55
125H_Q44	7.21	0.45	2.12×10^{-2}	3.34
H_Q15	3.22	0.75	2.55×10^{-2}	5.08
H_Q19	3.70	0.69	2.55×10^{-2}	4.60
H_Q22	4.20	0.64	2.55×10^{-2}	4.23
H_Q26	4.70	0.60	2.55×10^{-2}	3.91
H_Q30	5.21	0.56	2.53×10^{-2}	3.67
H_Q37	6.21	0.50	2.40×10^{-2}	3.37
H_Q44	7.21	0.45	2.22×10^{-2}	3.22
HB_Q15	3.25	0.75	2.88×10^{-2}	4.62
HB_Q19	3.73	0.69	2.89×10^{-2}	4.19
HB_Q22	4.22	0.64	2.87×10^{-2}	3.87
HB_Q26	4.72	0.60	2.83×10^{-2}	3.62
HB_Q30	5.22	0.56	2.77×10^{-2}	3.43

The relation of Eq. (16) is shown by the cyan dashed curve in Fig. 5. Comparing the curve describing Eq. (16) and the phase-space distribution of the matter at ≈ 1.5 ms after the onset of merger obtained by the simulation, we find a reasonable agreement between them in Fig. 5. Thus we consider that the model (assumption) given here is consistent with the result of the simulation. This can also be found in other models: In Figs. 6 and 7 we show the same quantity as Fig. 5 but for the models H_Q15 and H_Q37 at ≈ 1.5 ms and ≈ 15.0 ms after the onset of merger. For all the models shown in these figures, the relation described by Eq. (16) is consistent with the matter distribution at ≈ 1.5 ms after the onset of merger obtained by the simulations. All these results validate our model in terms of the effective potential for understanding the postmerger phase-space distribution of the matter.

The specific energy-angular momentum distribution of the matter with $\tilde{E} > 1$ at ≈ 15.0 ms after the onset of merger approximately agrees with the model given by Eq. (16). This implies that the ejecta component moves along the geodesic without any significant matter interaction, and the conservation of the specific energy and specific angular momentum is approximately satisfied.

Figures 5–7 also show the presence of the bound matter in a quasisteady state after merger. As found from the velocity distribution of the disk in the fourth panel of Fig. 1, a large portion of the disk matter is in a circular motion. The relation between the specific energy and
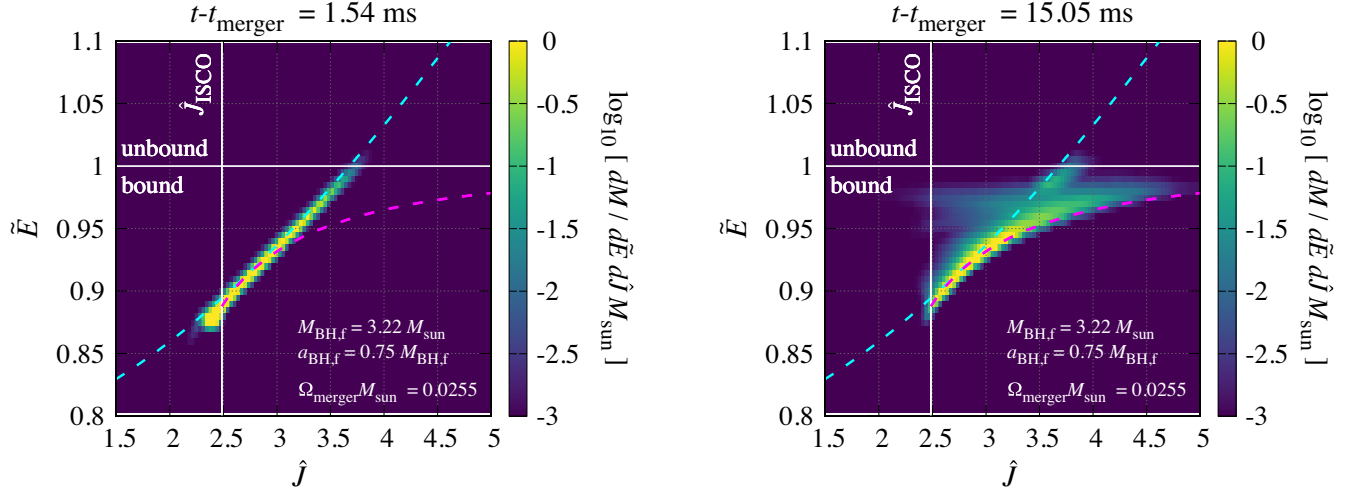
FIG. 6. The same as Fig. 5 but for model H_Q15 at $t - t_{\mathrm{merger}} \approx 1.5$, and 15.0 ms.

specific angular momentum for particles at stable circular orbits is given by [72]

$$\tilde{E}_{\mathrm{sco}}(\hat{r}) = \frac{\hat{r}^{3/2} - 2\hat{r}^{1/2} + \chi_{\mathrm{BH,f}}}{\hat{r}^{3/4}(\hat{r}^{3/2} - 3\hat{r}^{1/2} + 2\chi_{\mathrm{BH,f}})^{1/2}} \quad (\hat{r} > \hat{r}_{\mathrm{ISCO}}),$$

$$\hat{J}_{\mathrm{sco}}(\hat{r}) = \frac{+(\hat{r}^2 - 2\chi_{\mathrm{BH,f}}\hat{r}^{1/2} + \chi_{\mathrm{BH,f}}^2)}{\hat{r}^{3/4}(\hat{r}^{3/2} - 3\hat{r}^{1/2} + 2\chi_{\mathrm{BH,f}})^{1/2}} \quad (\hat{r} > \hat{r}_{\mathrm{ISCO}}), \quad (18)$$

where we assumed corotating orbits. Equation (18) is described by the magenta dashed curve in Figs. 5–7. The fourth panel of Fig. 5 shows that the curve describing Eq. (18) is consistent with the phase-space distribution of the disk matter for which the specific energy and specific angular momentum are $\tilde{E} \sim 0.9$–0.95 and $\hat{J} \sim 2.5$–3.5, respectively. It shows that the inner region of the disk is supported dominantly by rotation. However, there also exists the matter with the specific angular momentum appreciably smaller than $\hat{J}_{\mathrm{sco}}$ for the specific energy range

$\tilde{E} \sim 0.95$–1.0. We consider that the matter in the outer part of the disk has significant pressure support in addition to rotational support. These disk structures are consistent with that shown in Ref. [37]. For other models shown in Figs. 6 and 7, we also find the rotation-supported component and the component supported by both rotation and pressure at ≈ 15.0 ms after the onset of merger. Note that for the models H_Q15 (Fig. 6) and H_Q22 (Fig. 5), the former component is the majority, while for the model H_Q37 (Fig. 7), the latter component is the majority.

3. Dependence of the ejecta mass on the mass ratio

We describe our interpretation for the dependence of the ejecta mass on the mass ratio using the model for the matter distribution in the phase space and the distribution of matter with respect to the specific angular momentum normalized by the mass of the remnant black hole. Specifically, we compare the results of H_Q15, H_Q22, and H_Q37.
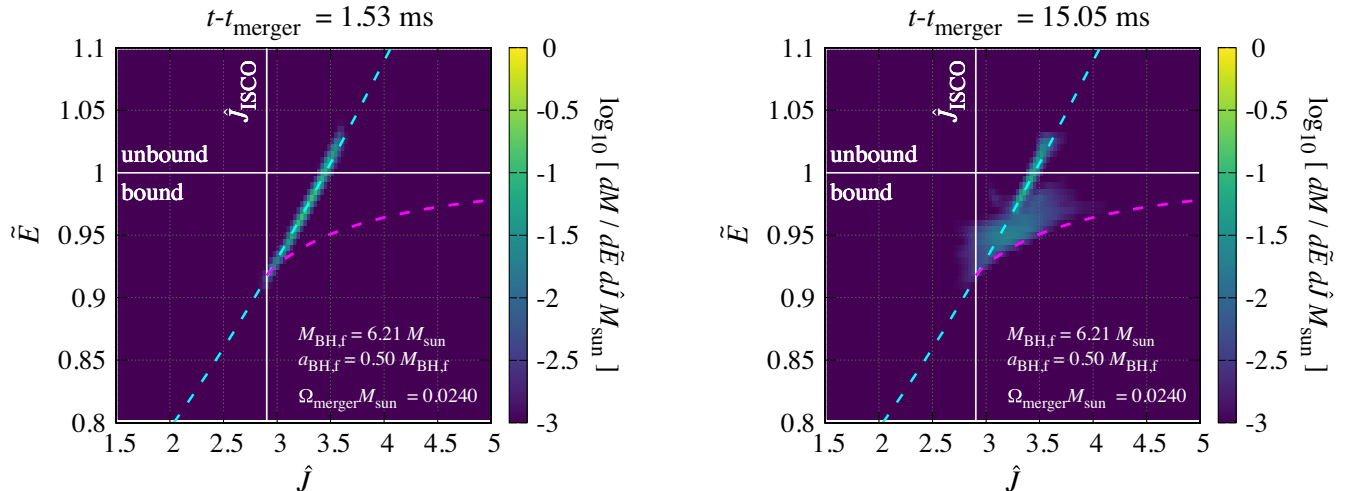

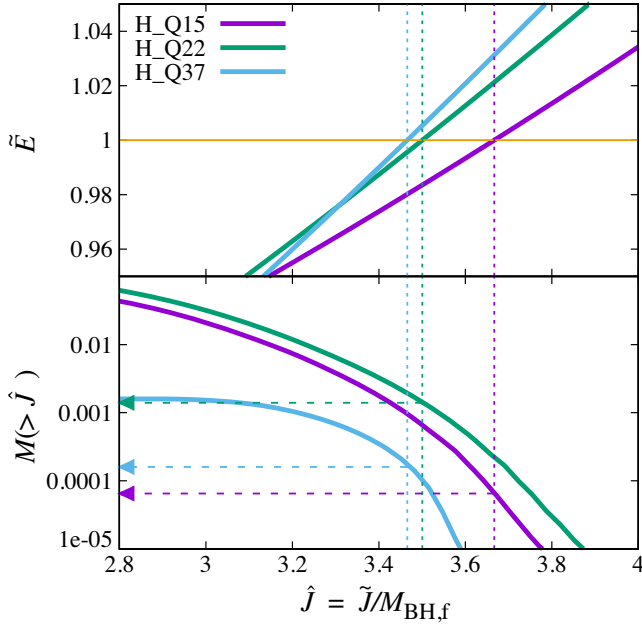FIG. 7. The same as Fig. 6 but for model H_Q37.

FIG. 8. The model for the matter distribution in the specific energy-angular momentum phase space given by Eq. (16) (top panel), and the specific angular momentum distribution obtained by applying Eq. (20) to numerical results of simulations at ≈ 1.5 ms after the onset of merger (bottom panel). The specific angular momentum is always normalized by the mass of the remnant black hole. We compare the results for H_Q15, H_Q22, and H_Q37. The horizontal line of $\tilde{E} = 1$ in the top panel is the boundary of bound and unbound matter. The specific angular momentum required for the matter to become ejecta $\hat{J}_{\rm crit}$ is described by the vertical dashed lines. As the mass ratio decreases, $\hat{J}_{\rm crit}$ increases. The horizontal arrows in the bottom panel show $M(> \hat{J}_{\rm crit})$ for each model. The mass-ratio dependence of $M(> \hat{J}_{\rm crit})$ is consistent with the mass-ratio dependence of the ejecta mass.

The top panel of Fig. 8 shows the mass-ratio dependence of the specific energy as a function of the specific angular momentum given by Eq. (16). This panel shows that as the mass ratio decreases, the specific angular momentum normalized by the remnant black-hole mass required for the matter to become ejecta (i.e., to achieve $\tilde{E} \geq 1$) increases. Here, the required specific angular momentum $\hat{J}_{\rm crit}$ is defined as

$$V_{\rm eff}(\hat{J}_{\rm crit}) = 1. \qquad (19)$$

$\hat{J}_{\rm crit}$ is also described in Fig. 8 by the vertical dashed lines. Here, the mass-ratio dependence of $\hat{r}_{\rm merger}$ is considered to be the main reason for the mass-ratio dependence of $\hat{J}_{\rm crit}$ (see Table V). The bottom panel of Fig. 8 shows the distribution of matter with respect to the specific angular momentum normalized by the mass of the remnant black hole $M(> \hat{J})$ at ≈ 1.5 ms after the onset of merger. Here, the distribution is obtained by the following integral:

$$M(> \hat{J}) := \int_{\hat{J}' > \hat{J}} \rho_*(\hat{J}') d^3 x. \qquad (20)$$

By comparing $M(> \hat{J})$ for H_Q15 and H_Q22, we find that the distribution does not differ significantly. On the other hand, the values of $M(> \hat{J})$ for H_Q37 is entirely smaller than that for other two models. The reason for this is the absence of appreciable tidal disruption for H_Q37.

The matter with specific angular momentum larger than $\hat{J}_{\rm crit}$ is expected to become ejecta, and thus the ejecta mass is estimated by $M(> \hat{J}_{\rm crit})$. $M(> \hat{J}_{\rm crit})$ is shown by the horizontal arrows in the bottom panel of Fig. 8. By comparing the curves of H_Q15 and H_Q22 we find that the ejecta mass should decrease as the mass ratio decreases. Here, the mass-ratio dependence of $\hat{J}_{\rm crit}$ is considered to be the main reason for the mass-ratio dependence of the ejecta mass for the low-mass-ratio regime. On the other hand, by comparing H_Q22 and H_Q37 we find that the ejecta mass should increase as the mass ratio decreases. In this case, the absence of appreciable tidal disruption for the high-mass-ratio models is the main reason for the mass-ratio dependence of the ejecta mass. This mass-ratio dependence of the ejecta mass is consistent with the results presented in Sec. III C. Quantitatively, the ejecta mass obtained from the analysis in Fig. 8, $M(> \hat{J}_{\rm crit})$, agrees with the actual results, $M_{\rm eje}$, within a factor of 2.

IV. CONCLUSION

We performed numerical relativity simulations for non-spinning low-mass black hole-neutron star mergers with seven black-hole masses (or mass ratios of the binary) and three neutron-star EOSs. We considered the cases in which the neutron-star mass is $1.35\,M_\odot$. We paid particular attention to the properties of the matter that remains outside the black hole including ejecta. We found that the rest mass of such matter is ~ 0.005–$0.1\,M_\odot$ for the case of $Q \lesssim 3$. Previous work [26] showed that the rest mass remaining outside the apparent horizon after the merger increases as the mass ratio decreases for $Q \gtrsim 3$. However, we found that it depends only weakly on the mass ratio for $Q \lesssim 3$.

Previous work [20] also showed that the ejecta mass increases as the mass ratio decreases for $Q \gtrsim 3$ with spinning black holes. In this work, we showed that the ejecta mass rapidly decreases as the mass ratio decreases for $Q \lesssim 3$. Because it is negligible for $Q \gtrsim 5$ with non-spinning black holes, the ejecta mass shows a peak at the mass ratio $Q \sim 3$. The peak value of the ejecta mass for models studied in this work was $\sim 10^{-3} - 5 \times 10^{-3}\,M_\odot$ depending on the neutron-star EOS. The average velocity of the ejecta extrapolated to $r \to \infty$ is found to be ~ 0.1–$0.2c$. It decreases as the mass ratio decreases, but the dependence on the neutron-star EOSs is weak.

In order to take a close look at the dynamics of the matter in the postmerger stage, we analyzed the matter distribution

in the phase space of the specific energy and the specific angular momentum. We found that the merger stage can be divided mainly into two stages. In the first stage, the matter acquires both energy and angular momentum as a result of angular momentum transport caused by the tidal deformation of the neutron star. In the second stage, the matter acquires energy, while there is only a small change in the specific angular momentum. We do not fully understand the physical mechanism for the second stage yet, but we speculate that the matter acquires energy due to the instantaneous change in the structure of the spacetime caused by the infall of the neutron-star matter into the black hole. As a result of these two stages, a portion of the matter that remains outside the black hole acquires sufficient energy to become ejecta.

The model for the matter distribution in the phase space suggests that the specific angular momentum normalized by the remnant black-hole mass required for the matter to become ejecta increases as the mass ratio of the binary decreases. In addition, we find that the distribution of matter with respect to the specific angular momentum normalized by the mass of the remnant black hole does not depend significantly on the mass ratio for a low-mass-ratio regime. Combining these two facts, we conclude that the ejecta mass decreases as the mass ratio decreases for the low mass-ratio binaries.

Finally, we list several issues to be explored in the future. In this paper, we studied the models only with nonspinning black holes. However, it is a well-known fact that the black-hole spin influences the merger process significantly [18,27]. We need further studies in order to clarify the parameter dependence of remnant disk and ejecta properties for low-mass black hole-neutron star mergers with a spinning black hole. Also, we plan to update the fitting formula for the rest mass remaining outside the apparent horizon after the merger and the ejecta mass by taking into account the results of this work.

ACKNOWLEDGMENTS

APPENDIX A: LOWER-RESOLUTION RESULTS AND CONVERGENCE

Tables VI–VIII compare characteristic quantities among different grid resolutions. These quantities are not always monotonic with respect to grid resolution. Such behavior is frequently seen in hydrodynamic quantities and they severely suffer low convergence order. One of the

TABLE VI. The rest mass outside the apparent horizon $M_{>\mathrm{AH}}[M_\odot]$ measured at 12 ms after the onset of merger for run with different grid resolution N110, N90, and N70. Errors with N110 results are also shown.

Model	N110	N90	N70	error[%]
125H_Q15	1.0×10^{-1}	1.0×10^{-1}	1.1×10^{-1}	15
125H_Q19	1.0×10^{-1}	1.0×10^{-1}	1.1×10^{-1}	9
125H_Q22	1.0×10^{-1}	1.1×10^{-1}	1.1×10^{-1}	13
125H_Q26	9.1×10^{-2}	9.5×10^{-2}	9.9×10^{-2}	15
125H_Q30	6.7×10^{-2}	7.1×10^{-2}	7.1×10^{-2}	9
125H_Q37	1.4×10^{-2}	1.1×10^{-2}	1.3×10^{-2}	3
125H_Q44	3.5×10^{-4}	7.2×10^{-4}	1.5×10^{-3}	>100
H_Q15	7.0×10^{-2}	7.2×10^{-2}	7.8×10^{-2}	18
H_Q19	7.3×10^{-2}	7.5×10^{-2}	7.7×10^{-2}	9
H_Q22	6.6×10^{-2}	6.9×10^{-2}	7.1×10^{-2}	14
H_Q26	4.4×10^{-2}	4.8×10^{-2}	4.9×10^{-2}	19
H_Q30	2.3×10^{-2}	2.4×10^{-2}	2.4×10^{-2}	3
H_Q37	1.3×10^{-3}	1.2×10^{-3}	2.7×10^{-3}	>100
H_Q44	$<10^{-5}$	1×10^{-5}	5×10^{-5}	…
HB_Q15	3.7×10^{-2}	3.5×10^{-2}	3.9×10^{-2}	10
HB_Q19	3.9×10^{-2}	3.8×10^{-2}	4.4×10^{-2}	23
HB_Q22	2.5×10^{-2}	3.1×10^{-2}	2.9×10^{-2}	32
HB_Q26	1.6×10^{-2}	1.5×10^{-2}	1.6×10^{-2}	2
HB_Q30	5.0×10^{-3}	4.1×10^{-3}	5.3×10^{-3}	10

TABLE VII. The same as Table VI but for the ejecta mass $M_{>\mathrm{eje}}[M_\odot]$.

Model	N110	N90	N70	error[%]
125H_Q15	3.7×10^{-4}	3.5×10^{-4}	3.2×10^{-4}	21
125H_Q19	1.5×10^{-3}	1.2×10^{-3}	1.1×10^{-3}	42
125H_Q22	2.9×10^{-3}	2.8×10^{-3}	4.8×10^{-3}	>100
125H_Q26	2.9×10^{-3}	5.1×10^{-3}	3.1×10^{-3}	9
125H_Q30	3.8×10^{-3}	4.3×10^{-3}	2.9×10^{-3}	38
125H_Q37	3.5×10^{-3}	2.0×10^{-3}	1.7×10^{-3}	88
125H_Q44	6×10^{-5}	2.1×10^{-4}	3.9×10^{-4}	>100
H_Q15	3×10^{-5}	5×10^{-5}	9×10^{-5}	>100
H_Q19	3.9×10^{-4}	3.1×10^{-4}	5.3×10^{-4}	61
H_Q22	8.8×10^{-4}	1.0×10^{-3}	9.6×10^{-4}	16
H_Q26	9.0×10^{-4}	1.6×10^{-3}	9.6×10^{-4}	13
H_Q30	2.0×10^{-3}	1.6×10^{-3}	8.5×10^{-4}	99
H_Q37	2.3×10^{-4}	1.4×10^{-4}	5.0×10^{-4}	>100
H_Q44	$<10^{-5}$	$<10^{-5}$	$<10^{-5}$	…
HB_Q15	$<10^{-5}$	1×10^{-5}	1×10^{-5}	…
HB_Q19	6.2×10^{-5}	3.7×10^{-5}	4.3×10^{-4}	>100
HB_Q22	9.7×10^{-5}	6.4×10^{-4}	1.8×10^{-4}	>100
HB_Q26	8.4×10^{-4}	3.9×10^{-4}	2.1×10^{-4}	>100
HB_Q30	5.2×10^{-4}	2.3×10^{-4}	2.0×10^{-4}	>100

TABLE VIII. The same as Table VI but for the average velocity of the ejecta extrapolated to $r \to \infty \, v_{\mathrm{eje,extrap}}[c]$. For low ejecta mass $< 10^{-5} \, M_\odot$, we do not estimate the ejecta velocity.

Model	N110	N90	N70	error[%]
125H_Q15	0.10	0.10	0.10	3
125H_Q19	0.12	0.12	0.12	13
125H_Q22	0.14	0.14	0.15	16
125H_Q26	0.14	0.16	0.14	3
125H_Q30	0.16	0.16	0.14	24
125H_Q37	0.18	0.15	0.15	36
125H_Q44	0.14	0.13	0.16	34
H_Q15	0.11	0.14	0.11	2
H_Q19	0.12	0.11	0.12	9
H_Q22	0.14	0.13	0.12	20
H_Q26	0.13	0.14	0.12	10
H_Q30	0.15	0.14	0.12	37
H_Q37	0.15	0.13	0.15	4
H_Q44	…	…	…	…
HB_Q15	…	0.18	0.30	…
HB_Q19	0.16	0.15	0.12	41
HB_Q22	0.11	0.14	0.11	4
HB_Q26	0.14	0.12	0.11	45
HB_Q30	0.14	0.12	0.12	27

reasons could be the discontinuous density gradient at the neutron star surface. Errors with N110 results are also shown in the tables. These errors are evaluated by assuming the first-order convergence between N110 and N70 results, considering that N110 and N90 are too close in resolution for evaluating errors. The mass ratio dependence and the EOS dependence of these quantities discussed in Sec. III B and Sec. III C remain robust in the range of the errors.

APPENDIX B: REST MASS REMAINING OUTSIDE THE APPARENT HORIZON AFTER THE MERGER FOR THE CASE OF HIGHER MASS RATIO AND SPINNING BLACK HOLE

Though it was not pointed out clearly, the weak mass-ratio dependence of the rest mass remaining outside the apparent horizon after the merger in a low mass-ratio regime can be seen for the merger of binaries consisting of spinning black holes from the results of previous simulations [18,20]. We reanalyzed the results of Refs. [18,20] focusing on the mass-ratio dependence. Figure 9 shows that the mass-ratio dependence of the rest mass located outside the apparent horizon tends to be weaker as the mass ratio decreases for models
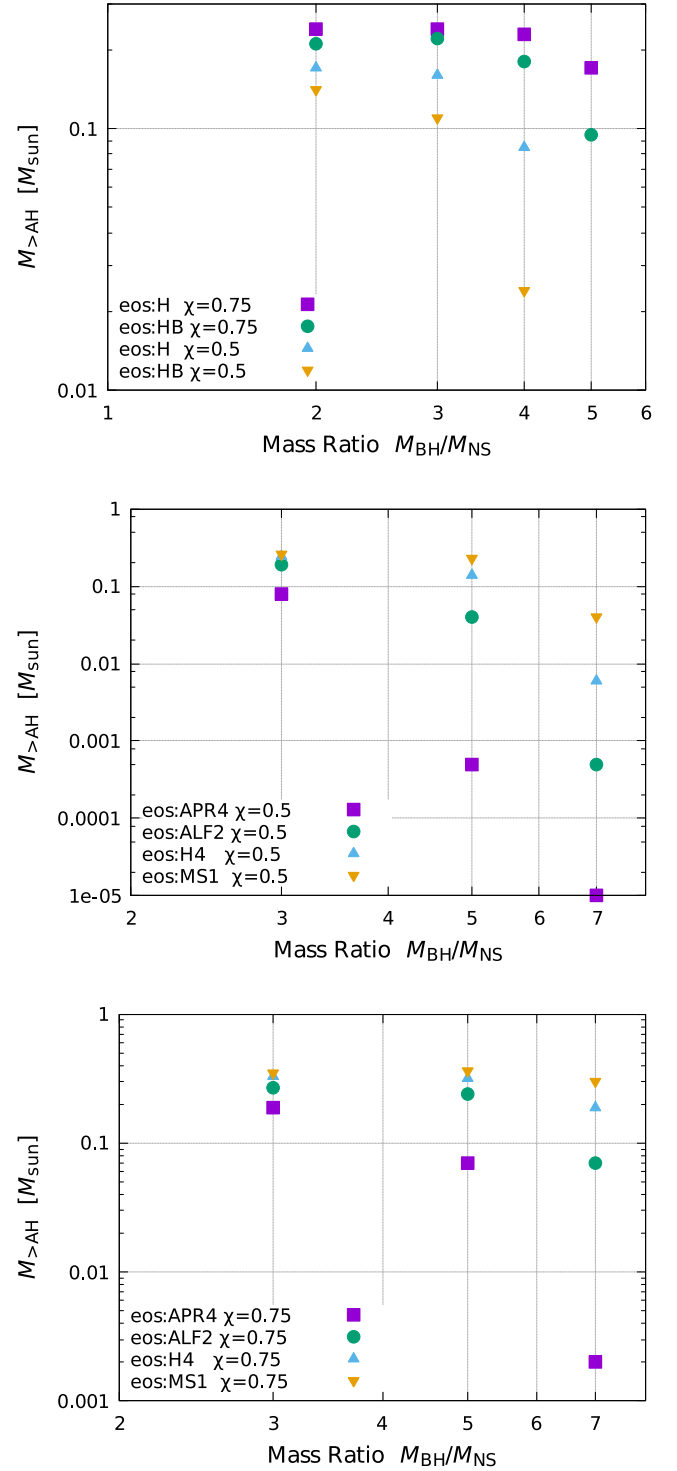

FIG. 9. Dependence of the rest mass remaining outside the apparent horizon after the merger on the mass ratio for binaries with spinning black holes. In each panel, EOSs and spin parameters are aligned. The data are taken from Ref. [18] (top panel) and Ref. [20] (middle and bottom panels). The compactness of the neutron star with a mass $1.35 \, M_\odot$ is 0.138, 0.147, 0.161, and 0.180 for EOSs MS1, H4, ALF2, and APR4, respectively.

with higher black-hole spins and stiffer neutron-star EOSs. It should not be off base to expect the same tendency for models with lower black-hole spins and softer neutron-star EOSs in the mass-ratio regime lower than the scope of Refs. [18,20]. We expect that this is a universal behavior irrespective of the black-hole spin. It should also be noted that the mass ratio at which the rest mass remaining outside the apparent horizon after the merger starts leveling off depends on the compactness of the neutron star (or neutron-star EOS) and the black-hole spin. It is also worth noting that Ref. [43] pointed out that the rest mass remaining outside the apparent horizon after the merger does not depend strongly on the compactness of the neutron star for binary systems with $\chi_{BH} = 0.9$, which results in a massive disk.

[1] B. P. Abbott *et al.* (LIGO Scientific and Virgo Collaborations), Phys. Rev. Lett. **116**, 061102 (2016).

[2] B. P. Abbott *et al.* (LIGO Scientific and Virgo Collaborations), Phys. Rev. Lett. **119**, 161101 (2017).

[3] B. P. Abbott *et al.*, Astrophys. J. **848**, L12 (2017).

[4] B. P. Abbott *et al.*, Astrophys. J. **848**, L13 (2017).

[5] B. P. Abbott *et al.* (LIGO Scientific and Virgo Collaborations), Phys. Rev. X **9**, 011001 (2019).

[6] F. Foucart, M. D. Duez, L. E. Kidder, S. M. Nissanke, H. P. Pfeiffer, and M. A. Scheel, Phys. Rev. D **99**, 103025 (2019).

[7] T. Hinderer, S. Nissanke, F. Foucart, K. Hotokezaka, T. Vincent, M. Kasliwal, P. Schmidt, A. R. Williamson, D. A. Nichols, M. D. Duez, L. E. Kidder, H. P. Pfeiffer, and M. A. Scheel, Phys. Rev. D **100**, 063021 (2019).

[8] B. P. Abbott *et al.*, Astrophys. J. **892**, L3 (2020).

[9] K. Kyutoku, S. Fujibayashi, K. Hayashi, K. Kawaguchi, K. Kiuchi, M. Shibata, and M. Tanaka, Astrophys. J. **890**, L4 (2020).

[10] M.-Z. Han, S.-P. Tang, Y.-M. Hu, Y.-J. Li, J.-L. Jiang, Z.-P. Jin, Y.-Z. Fan, and D.-M. Wei, Astrophys. J. **891**, L5 (2020).

[11] B. P. Abbott *et al.* (LIGO Scientific and Virgo Collaborations), Phys. Rev. X **9**, 031040 (2019).

[12] R. Abbott *et al.*, arXiv:2010.14527 [Phys. Rev. X (to be published)].

[13] L.-X. Li and B. Paczyski, Astrophys. J. **507**, L59 (1998).

[14] B. D. Metzger, G. Martnez-Pinedo, S. Darbha, E. Quataert, A. Arcones, D. Kasen, R. Thomas, P. Nugent, I. V. Panov, and N. T. Zinner, Mon. Not. R. Astron. Soc. **406**, 2650 (2010).

[15] E. Nakar, Phys. Rep. **442**, 166 (2007).

[16] E. Berger, Annu. Rev. Astron. Astrophys. **52**, 43 (2014).

[17] K. Kyutoku, M. Shibata, and K. Taniguchi, Phys. Rev. D **82**, 044049 (2010).

[18] K. Kyutoku, H. Okawa, M. Shibata, and K. Taniguchi, Phys. Rev. D **84**, 064018 (2011).

[19] K. Kyutoku, K. Ioka, and M. Shibata, Phys. Rev. D **88**, 041503 (2013).

[20] K. Kyutoku, K. Ioka, H. Okawa, M. Shibata, and K. Taniguchi, Phys. Rev. D **92**, 044028 (2015).

[21] M. Shibata and K. Uryū, Phys. Rev. D **74**, 121503 (2006).

[22] M. Shibata and K. Taniguchi, Phys. Rev. D **77**, 084015 (2008).

[23] M. Shibata and K. Uryū, Classical Quantum Gravity **24**, S125 (2007).

[24] Z. B. Etienne, J. A. Faber, Y. T. Liu, S. L. Shapiro, K. Taniguchi, and T. W. Baumgarte, Phys. Rev. D **77**, 084002 (2008).

[25] M. D. Duez, F. Foucart, L. E. Kidder, H. P. Pfeiffer, M. A. Scheel, and S. A. Teukolsky, Phys. Rev. D **78**, 104015 (2008).

[26] M. Shibata, K. Kyutoku, T. Yamamoto, and K. Taniguchi, Phys. Rev. D **79**, 044030 (2009).

[27] Z. B. Etienne, Y. T. Liu, S. L. Shapiro, and T. W. Baumgarte, Phys. Rev. D **79**, 044024 (2009).

[28] S. Chawla, M. Anderson, M. Besselman, L. Lehner, S. L. Liebling, P. M. Motl, and D. Neilsen, Phys. Rev. Lett. **105**, 111101 (2010).

[29] M. D. Duez, F. Foucart, L. E. Kidder, C. D. Ott, and S. A. Teukolsky, Classical Quantum Gravity **27**, 114106 (2010).

[30] F. Foucart, M. D. Duez, L. E. Kidder, and S. A. Teukolsky, Phys. Rev. D **83**, 024005 (2011).

[31] F. Foucart, M. D. Duez, L. E. Kidder, M. A. Scheel, B. Szilagyi, and S. A. Teukolsky, Phys. Rev. D **85**, 044015 (2012).

[32] Z. B. Etienne, Y. T. Liu, V. Paschalidis, and S. L. Shapiro, Phys. Rev. D **85**, 064029 (2012).

[33] Z. B. Etienne, V. Paschalidis, and S. L. Shapiro, Phys. Rev. D **86**, 084026 (2012).

[34] F. Foucart, M. B. Deaton, M. D. Duez, L. E. Kidder, I. MacDonald, C. D. Ott, H. P. Pfeiffer, M. A. Scheel, B. Szilagyi, and S. A. Teukolsky, Phys. Rev. D **87**, 084006 (2013).

[35] G. Lovelace, M. D. Duez, F. Foucart, L. E. Kidder, H. P. Pfeiffer, M. A. Scheel, and B. Szilágyi, Classical Quantum Gravity **30**, 135004 (2013).

[36] M. B. Deaton, M. D. Duez, F. Foucart, E. O'Connor, C. D. Ott, L. E. Kidder, C. D. Muhlberger, M. A. Scheel, and B. Szilagyi, Astrophys. J. **776**, 47 (2013).

[37] F. Foucart, M. B. Deaton, M. D. Duez, E. O'Connor, C. D. Ott, R. Haas, L. E. Kidder, H. P. Pfeiffer, M. A. Scheel, and B. Szilagyi, Phys. Rev. D **90**, 024026 (2014).

[38] V. Paschalidis, M. Ruiz, and S. L. Shapiro, Astrophys. J. **806**, L14 (2015).

[39] K. Kawaguchi, K. Kyutoku, H. Nakano, H. Okawa, M. Shibata, and K. Taniguchi, Phys. Rev. D **92**, 024014 (2015).

[40] K. Kiuchi, Y. Sekiguchi, K. Kyutoku, M. Shibata, K. Taniguchi, and T. Wada, Phys. Rev. D **92**, 064034 (2015).

[41] F. Foucart, D. Desai, W. Brege, M. D. Duez, D. Kasen, D. A. Hemberger, L. E. Kidder, H. P. Pfeiffer, and M. A. Scheel, Classical Quantum Gravity **34**, 044002 (2017).

[42] K. Kyutoku, K. Kiuchi, Y. Sekiguchi, M. Shibata, and K. Taniguchi, Phys. Rev. D **97**, 023009 (2018).

[43] W. Brege, M. D. Duez, F. Foucart, M. B. Deaton, J. Caro, D. A. Hemberger, L. E. Kidder, E. O'Connor, H. P. Pfeiffer, and M. A. Scheel, Phys. Rev. D **98**, 063009 (2018).

[44] M. Ruiz, S. L. Shapiro, and A. Tsokaros, Phys. Rev. D **98**, 123017 (2018).

[45] F. Foucart, M. D. Duez, T. Hinderer, J. Caro, A. R. Williamson, M. Boyle, A. Buonanno, R. Haas, D. A. Hemberger, L. E. Kidder, H. P. Pfeiffer, and M. A. Scheel, Phys. Rev. D **99**, 044008 (2019).

[46] F. Özel, D. Psaltis, R. Narayan, and A. Santos Villarreal, Astrophys. J. **757**, 55 (2012).

[47] T. A. Thompson, C. S. Kochanek, K. Z. Stanek, C. Badenes, R. S. Post, T. Jayasinghe, D. W. Latham, A. Bieryla, G. A. Esquerdo, P. Berlind, M. L. Calkins, J. Tayar, L. Lindegren, J. A. Johnson, T. W.-S. Holoien, K. Auchettl, and K. Covey, Science **366**, 637 (2019).

[48] R. Abbott *et al.*, Astrophys. J. **896**, L44 (2020).

[49] GraceDB, https://gracedb.ligo.org/superevents/public/O3/.

[50] K. Kiuchi, K. Kawaguchi, K. Kyutoku, Y. Sekiguchi, M. Shibata, and K. Taniguchi, Phys. Rev. D **96**, 084060 (2017).

[51] T. Yamamoto, M. Shibata, and K. Taniguchi, Phys. Rev. D **78**, 064054 (2008).

[52] M. Campanelli, C. O. Lousto, P. Marronetti, and Y. Zlochower, Phys. Rev. Lett. **96**, 111101 (2006).

[53] J. G. Baker, J. Centrella, D.-I. Choi, M. Koppitz, and J. van Meter, Phys. Rev. Lett. **96**, 111102 (2006).

[54] P. Marronetti, W. Tichy, B. Brügmann, J. González, and U. Sperhake, Phys. Rev. D **77**, 064010 (2008).

[55] M. Shibata and T. Nakamura, Phys. Rev. D **52**, 5428 (1995).

[56] T. W. Baumgarte and S. L. Shapiro, Phys. Rev. D **59**, 024007 (1998).

[57] D. Hilditch, S. Bernuzzi, M. Thierfelder, Z. Cao, W. Tichy, and B. Brügmann, Phys. Rev. D **88**, 084057 (2013).

[58] J. M. Lattimer and M. Prakash, Science **304**, 536 (2004).

[59] J. S. Read, B. D. Lackey, B. J. Owen, and J. L. Friedman, Phys. Rev. D **79**, 124032 (2009).

[60] J. S. Read, C. Markakis, M. Shibata, K. Uryū, J. D. E. Creighton, and J. L. Friedman, Phys. Rev. D **79**, 124033 (2009).

[61] B. D. Lackey, K. Kyutoku, M. Shibata, P. R. Brady, and J. L. Friedman, Phys. Rev. D **85**, 044061 (2012).

[62] H. T. Cromartie, E. Fonseca, S. M. Ransom, P. B. Demorest, Z. Arzoumanian, H. Blumer, P. R. Brook, M. E. DeCesar, T. Dolch, J. A. Ellis *et al.*, Nat. Astron. **4**, 7276 (2019).

[63] K. Kyutoku, M. Shibata, and K. Taniguchi, Phys. Rev. D **79**, 124018 (2009).

[64] L. Bildsten and C. Cutler, Astrophys. J. **400**, 175 (1992).

[65] C. S. Kochanek, Astrophys. J. **398**, 234 (1992).

[66] C. O. Lousto, H. Nakano, Y. Zlochower, and M. Campanelli, Phys. Rev. D **82**, 104057 (2010).

[67] C. Reisswig and D. Pollney, Classical Quantum Gravity **28**, 195015 (2011).

[68] M. Shibata and K. Taniguchi, Living Rev. Relativity **14**, 6 (2011).

[69] F. Foucart, Phys. Rev. D **86**, 124007 (2012).

[70] K. Kawaguchi, K. Kyutoku, M. Shibata, and M. Tanaka, Astrophys. J. **825**, 52 (2016).

[71] R. Ruffini and J. A. Wheeler, ESRO **52**, 45 (1971), https://ui.adsabs.harvard.edu/abs/1971ESRSP..52...45R/abstract.

[72] J. M. Bardeen, W. H. Press, and S. A. Teukolsky, Astrophys. J. **178**, 347 (1972).